Research Article | Vol. 28, No. 24 / 23 November 2020 / Optics Express 35695
Optics EXPRESS

Polarization independent enhancement of zeroth order diffracted second harmonic from multilayer gallium selenide on a silicon resonant metasurface

JAYANTA DEKA, MEDHA DANDU, LAL KRISHNA A. S., SRUTI MENON, K. M. JYOTHSNA, RABINDRA BISWAS, KAUSIK MAJUMDAR, AND VARUN RAGHUNATHAN*

Department of Electrical Communication Engineering, Indian Institute of Science, Bangalore, India
varunr@iisc.ac.in

Abstract: We demonstrate polarization-independent resonant-enhancement of second harmonic generation (SHG) from multilayer Gallium Selenide (GaSe) on a silicon-based resonant metasurface. Two-dimensional hexagonal photonic lattice with circularly symmetric silicon meta-atoms are designed to achieve resonant field enhancement at the fundamental wavelength independent of the incident polarization direction. Such structures are however found to exhibit strong resonant field depolarization effects at the fundamental excitation fields resulting in modified nonlinear polarization components when compared to the native GaSe layer. Furthermore, the sub-wavelength metasurface designed to have resonances at the fundamental wavelengths act as a higher order diffraction grating at the second harmonic wavelength. Nonlinear wave propagation simulations show that the higher order diffracted SHG exhibit strong polarization dependent enhancement with characteristics very different from the native GaSe layer. In this context, polarization independent enhancement of the second harmonic signal is achieved only for the zeroth order diffracted component. Experimental study of second harmonic generation from the GaSe layer integrated with the silicon metasurface shows maximum nonlinear signal enhancement on-resonance with polarization dependence identical to the native GaSe layer by selectively detecting the zeroth-order diffracted component. This work shows that it is not sufficient to use symmetric meta-atoms in such 2D material integrated resonant metasurfaces for achieving polarization independent nonlinear optical enhancement. Depolarization of the resonant fields and higher-order diffraction at the nonlinear signal wavelength need to be considered as well.

1. Introduction

Dielectric metasurfaces are finding numerous applications for controlling light-matter interactions at the nanoscale. This is due to the low optical absorption losses, high damage thresholds and the ability to engineer the field profiles to be located either inside or evanescently extend outside the structures [1,2]. In the linear regime, control over the amplitude, phase and polarization properties of the transmitted light is utilized for realizing phased arrays, flat lenses, holograms etc [3–8]. In the nonlinear regime, the resonant field enhancement in the metasurfaces is utilized for enhancing harmonic generation, wave-mixing and optical switching processes [9–11]. Resonant dielectric metasurfaces composed of one-dimensional (1D) or two-dimensional (2D) sub-wavelength high-contrast gratings [12], partially etched structures in the form of zero-contrast gratings [13,14], and structures supporting Fano resonances through the coupling of bright and dark modes [10] have been studied previously for nonlinear optical enhancement. Isolated particles and multiparticle oligomeric units supporting Mie resonances have also been used for resonant scattering and nonlinear optical studies [15–17]. For the above described structures,

#405524 https://doi.org/10.1364/OE.405524
Journal © 2020 Received 17 Aug 2020; revised 28 Oct 2020; accepted 28 Oct 2020; published 10 Nov 2020

Optics EXPRESS

the dielectric materials used to realize the spectral resonances act as the active nonlinear media. Recently, there is also extensive interest in studying nonlinear optical properties of monolayer and few-layer 2D materials [18]. However, the inherent ultrathin 2D material limits the overall nonlinear optical efficiency due to reduced interaction length. To overcome this limitation, 2D materials are integrated with resonant photonic structures to increase the overall nonlinear optical interaction strength. Such heterogenously integrated structures offer the advantage of combining a range of 2D materials exhibiting diverse linear and nonlinear optical properties with prefabricated photonic structures using simple dry-transfer or chemical vapor deposition techniques [18]. Previous work on nonlinear optics in 2D material integrated with resonant cavity structures include second harmonic generation enhancement from transition metal dichalcogenide (TMDC) layers integrated with photonic crystals defect cavities [19–21], resonant distributed brag-reflector cavities [22,23] and metallic 1D grating structures [24]. In the context of dielectric metasurfaces, resonant enhancement of second-harmonic and sum-frequency generation on Gallium Selenide (GaSe) flake coupled to L-shaped asymmetric 2D silicon metasurface [25] has been reported. A theoretical study of second-harmonic generation enhancement from TMDC monolayer on 1D gratings utilizing bound-states in the continuum resonance [26] has also been reported. The resonant enhancement using 1D, asymmetric 2D metasurfaces and photonic crystal defect cavities are inherently polarization sensitive as the cavity selectively enhances one specific incident light polarization. This leads to the overall 2D material-metasurface system exhibiting different polarization characteristics when compared to the inherent 2D material. This also leads to the requirement of careful alignment of the crystal axis of the 2D material with the metasurface axis to maximize the resonant nonlinear optical process. It would be desirable to de-couple the polarization properties of the 2D material from the underlying metasurface to realize a generic heterogeneously integrated 2D material-resonant metasurface platform.

In this paper, we experimentally report for the first time to the best of our knowledge, polarization-independent enhancement of second-harmonic generation (SHG) from two-dimensional material heterogenously integrated with resonant metasurface. We report this in multilayer GaSe integrated with silicon resonant metasurface. GaSe is a particularly promising material for integration with metasurfaces due to its large inherent second order susceptibility, which is approximately two orders of magnitude higher than other popular TMDC monolayers [18,27]. Furthermore, the prevalent ε-GaSe form is found to be non-centrosymmetric irrespective of the number of layers, giving rise to quadratic increase in SHG signal with thickness [28,29]. In this work, resonant metasurface comprising of 2D hexagonal lattice of silicon sub-wavelength structures with circularly symmetric meta-atoms are designed to achieve resonant fields at the fundamental wavelength which follow the incident polarization direction. It is found that the resonant electric field at the fundamental wavelength exhibits significant depolarization effects, i.e. the presence of non-negligible orthogonal field components to the incident polarization direction. This results in modified nonlinear polarization components from the GaSe layer above the metasurface when compared to the native GaSe layer. Furthermore, the resonant metasurface designed to operate in the zeroth order diffraction regime at the fundamental wavelength exhibit higher order diffraction at the second harmonic wavelength resulting in SHG emission being distributed across multiple diffraction orders. Through nonlinear wave propagation simulations, it is found that the higher order diffracted SHG exhibit strong polarization dependence which departs significantly from that of the native GaSe layer. Only the zeroth order diffracted SHG is found to exhibit polarization dependence identical to the native GaSe layer. Experimental studies on multilayer GaSe dry-transferred to resonant metasurfaces fabricated on silicon-on-insulator substrate results in SHG enhancement of ~22 times on top of the metasurface close to the fundamental resonance wavelength. The polarization studies of the detected SHG signal on-resonance show identical dependence both above and away from the metasurface, confirming the polarization independent

Optics EXPRESS

nature of SHG enhancement when restricting the light collection to only the zeroth-order diffraction component.

2. Design studies

A schematic of the 2D material – resonant metasurface system considered in this paper is shown in Fig. 1. The silicon high-index contrast structures consist of fully etched sub-wavelength circular pillars arranged in a 2-D hexagonal array on a silicon-on-insulator (SOI) substrate. The individual meta-atoms are chosen to be circularly symmetric to achieve polarization-independent fundamental field excitation (shown by the red arrow at frequency ω). The second harmonic generation signal (shown by the blue arrows at frequency 2ω) is generated from the 2D material transferred on top of the resonant metasurface. The structures are designed to operate in the zeroth order diffraction regime for the fundamental excitation, resulting in higher-order diffraction for the second-harmonic wavelength. The lab co-ordinate system (shown by the black solid axes – x,y,z) and the crystal co-ordinate system (shown by black dashed axes x′, y′ rotated in the xy plane by an angle ϕ) are also shown in Fig. 1. The incident light polarization is at an angle θ with respect to the x-axis in the xy plane (shown by the red colored double-headed arrow).

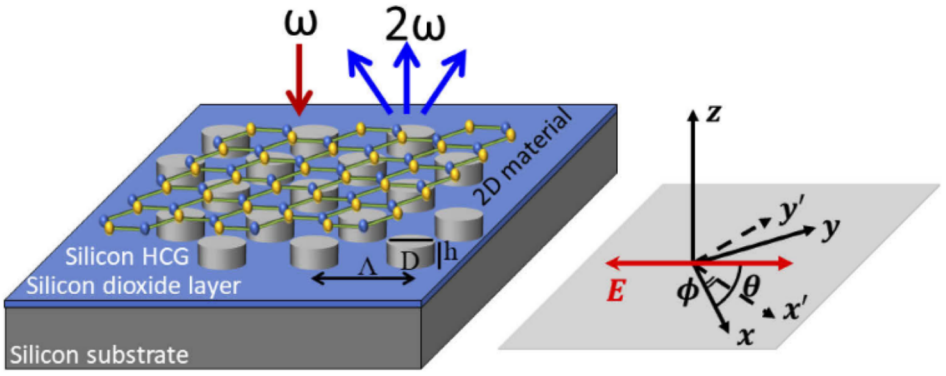

Fig. 1. Schematic of the 2D material overlaid on top of the resonant metasurface for polarization-independent enhancement of second harmonic generation. The x,y,z lab co-ordinate system (black solid axes), the x′,y′ crystal co-ordinate system (black dashed axes) and the incident electric field direction (red colored doubled-headed arrow) are also shown.

The simulated transmission spectra contour map as a function of varying pillar diameter (varying from 400 to 900 nm) is shown in Fig. 2(a) for a fixed height, h = 220 nm and pitch, Λ = 1.2 μm. The electromagnetic simulations are performed using rigorous coupled-wave analysis method (RCWA) using S4 [30], with plane wave excitation at normal incidence. The separation between the sub-wavelength, zeroth-order diffraction region exhibiting prominent high contrast resonant features and the higher order diffraction region exhibiting lower contrast transmission features is marked by the vertical dashed line (corresponds to a wavelength of $\frac{\sqrt{3}}{2}\Lambda.n_{substrate} \approx 1.51$ μm) [31]. In the zeroth order diffraction region, two prominent resonance features with transmission minima are observed in the 1500 to 1700 nm wavelength range. The design window of interest here considering the ease of patterning the features with pillar diameter, D in the range of 600-700 nm (resulting in duty-cycle of 50-60%) is also indicated in Fig. 2(a). Specifically, for D = 660 nm, the transmission spectrum over a narrower spectral region is shown (blue curve) in Fig. 2(b). The effect of varying incidence angles is also shown in Fig. 2(b). Resonance features are found to red-shift with increasing incidence angle with the appearance of other prominent resonances within a spectral window of 40 nm for 8° acceptance angle. This spectral range is comparable to the typical spectral width of an ultrafast laser source with 100-200

Optics EXPRESS

fsec pulse-width used as the fundamental excitation in the 1500-1600 nm range. Figure 2(c) shows the transmission spectra as a function of varying GaSe layer thickness added on top of the silicon structures. The refractive index of GaSe is fitted with the model provided in K. Kato et. al. [32]. The resonance transmission dip is found to red-shift by ~15, 25 and 50 nm in the presence of the GaSe layer of thickness 5, 10 and 15 nm respectively. The quality factor of the resonance under consideration is estimated to be ~48 for 10 nm GaSe layer. A slight spectral narrowing is also observed in the presence of the GaSe layer on top of the metasurface [25].

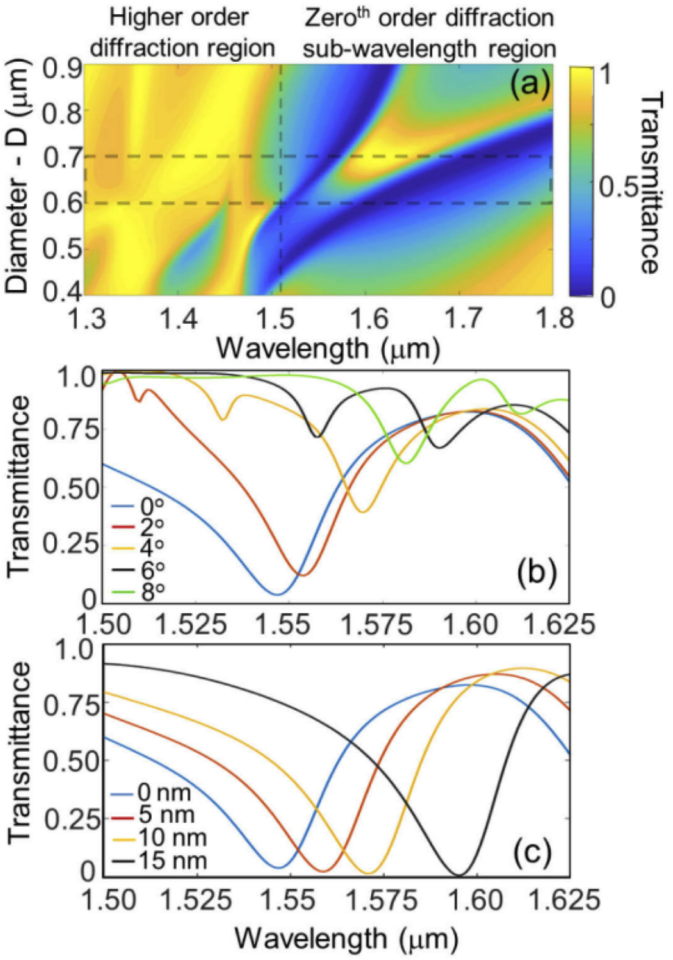

Fig. 2. Design of silicon metasurface and effect of GaSe layer. (a) Transmission spectra contour map for varying circular pillar diameter. The pitch and height of the structure are fixed as 1.2 μm and 220 nm respectively. The transition from the zeroth-order diffraction region and higher order diffraction region is shown by the vertical dashed line. Transmission spectrum for silicon pillar diameter of 600-700 nm is shown by the dashed box. (b) Transmission spectra simulated for fixed diameter of 660 nm for varying angles of incidence for fundamental excitation. (c) Transmission spectra simulated for varying thickness of GaSe integrated on top of the silicon metasurface.

The xy electric field amplitude profiles obtained at the middle of a 10 nm GaSe layer placed above the metasurface are shown in Figs. 3(a)–3(d). The incident light at the resonance wavelength of 1572 nm with linear x-polarization is considered. The dominant field component in the GaSe

Optics EXPRESS

layer is found to be x-polarized with a double-lobed profile and field enhancement of ~8 times. The orthogonal y-polarized field component with a four-lobed profile and field enhancement of ~5 times is also observed. There is also a non-negligible longitudinal, z-polarized field component observed with field enhancement of ~3 times. This depolarization effect in the resonant electric field, with ratio of x and y-components of ~1.6:1 arises due to the interaction of a normal incidence plane wave excitation with the resonant structures. Similar field depolarization effects are observed in non-paraxial focal fields created by focusing light using high numerical aperture objective lenses with numerical aperture comparable to or greater than unity and with the use of radially polarized incident light [33]. The designed 2D metasurface with circularly-symmetric meta-atoms results in resonant field in the structure which rotates with the incident polarization direction. However, the effect of depolarization needs to be considered for calculating the second-order nonlinear polarization for the SHG process. ε-GaSe crystal having D_{3h} symmetry [27–29], has the following non-vanishing $\chi^{(2)}$ elements [34]: x′x′x′ = -x′y′y′ = -y′y′x′ = -y′x′y′, where x′ and y′ denote the arm-chair and zig-zag crystallographic axes respectively (shown in Fig. 1). From the non-zero susceptibility elements it is evident that the z-component of the field plays no role in generating the nonlinear polarization. For the incident electric field, E polarized at an angle θ with respect to the lab x-axis, the resonant field in the structure can be resolved along the arm-chair and zig-zag directions as: $E_{x'} = E_{\parallel}.\mathrm{Cos}(\theta - \phi) - E_{\perp}.Sin(\theta - \phi)$ and $E_{y'} = E_{\parallel}.\mathrm{Sin}(\theta - \phi) + E_{\perp}.Cos(\theta - \phi)$. $E_{\parallel}$ and $E_{\perp}$ represent the resonant field components in the structure parallel and perpendicular to the incident field direction, respectively. The nonlinear polarization components along the arm-chair and zig-zag axes can be written as: $P^{(2)}_{x'} = \varepsilon_0 \chi^{(2)}_{x'x'x'}({E_{x'}}^2 - {E_{y'}}^2)$ and $P^{(2)}_{y'} = -2\varepsilon_0 \chi^{(2)}_{x'x'x'} E_{x'} E_{y'}$. The projection of the nonlinear polarization along the x and y directions are obtained as follows:

$$P^{(2)}_x = \varepsilon_o \chi^{(2)}_{x'x'x'}[(E^2_{\parallel} - E^2_{\perp}).\mathrm{Cos}(2\theta - 3\phi) - 2E_{\parallel}E_{\perp}.\mathrm{Sin}(2\theta - 3\phi)] \quad (1)$$

$$P^{(2)}_y = -\varepsilon_o \chi^{(2)}_{x'x'x'}[(E^2_{\parallel} - E^2_{\perp}).\mathrm{Sin}(2\theta - 3\phi) + 2E_{\parallel}E_{\perp}.\cos(2\theta - 3\phi)] \quad (2)$$

Figures 3(e)–3(g) show the second-order nonlinear polarization profiles for the case in which the incident electric field polarization and arm-chair axis aligned along the x direction (θ=0, ϕ=0). It is found that the depolarization results in non-zero nonlinear polarization components along both x and y lab axes. The x and y components exhibit two-lobe and four-lobe profiles respectively due to the dominant nonlinear polarization terms being proportional to $E^2_{\parallel}$ and $E_{\parallel}E_{\perp}$, in Eqs. (1) and (2). For comparison, the second-order nonlinear polarization for the case of the native GaSe layer and negligible depolarization effect (i.e. $E_{\perp} = 0$) simplifies the above equations to $E^2_{\parallel}.\cos(2\theta - 3\phi)$ and $E^2_{\parallel}.\mathrm{Sin}(2\theta - 3\phi)$ dependence for the x- and y-polarization components respectively. This results in the frequently reported six-fold symmetry for the polar plot when the SHG signal is collected along the parallel and perpendicular directions to the incident polarization direction [35]. The SHG wave propagation from the GaSe layer considering the interaction with the silicon metasurface is modeled in COMSOL by solving for the nonlinear-wave propagation equation [34]:

$$\nabla \times \mu_r^{-1}(\nabla \times E) - {k_0}^2 \varepsilon_r E = \omega^2 \mu_0 P \quad (3)$$

The nonlinear polarization calculated in Eqs. (1) and (2) act as the driving field for the generation and propagation of the second-harmonic wave. Figure 4(a) shows that xz cross-sectional electric field calculated at the SHG wavelength. The interaction of the SHG electric field with the silicon metasurface and its propagation in the forward and backward directions are shown in Fig. 4(a).

The periodicity of the metasurface elements is chosen to ensure that the fundamental excitation wave is resonantly enhanced in the zeroth order diffraction regime, as shown in Fig. 2(a). This however results in the generated second harmonic experiencing higher order diffraction as it propagates from the nonlinear medium. For plane wave excitation at the fundamental wavelength and infinitely extended metasurface, the various diffraction orders at the SHG wavelength are

Optics EXPRESS

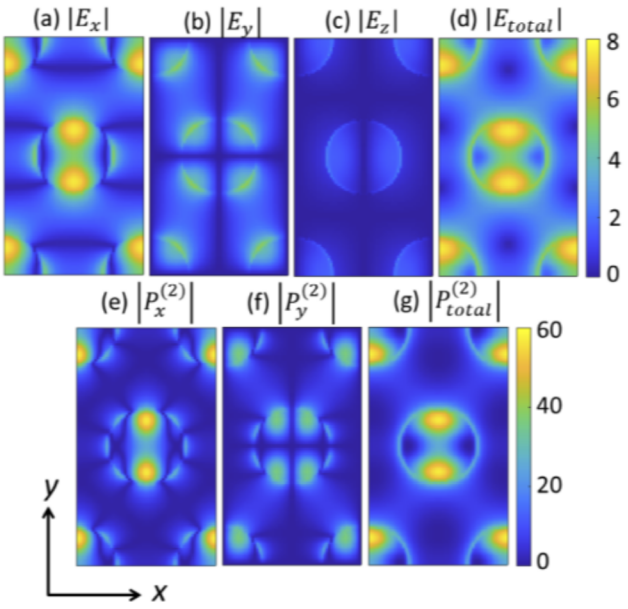

Fig. 3. Electric field amplitude profiles at the fundamental excitation resonance at 1572 nm shown at the GaSe layer for: (a) x, (b) y, (c) z components, and (d) total combined. Calculated nonlinear polarization amplitude profiles for the SHG process at 786 nm for: (e) x, (f) y components, and (g) total combined. The plots are shown across a rectangular unit-cell of dimensions 1.2×2.08 μm.

treated as plane-waves propagating with different wave-vector directions and polarized parallel (in-plane) or perpendicular (out-of-plane) to the plane of diffraction, defined as the plane containing the optical axis (along z-axis) and diffracted wave-vector. The field amplitude coefficients are calculated by projecting the electric field, E(2ω) onto the different diffraction-order basis functions, E_i as: [36]

$$S_i = \frac{\int E(2\omega).E_i^* dA}{\int E_i.E_i^* dA} \tag{4}$$

The diffraction efficiency for each order can be calculated as $|S_i|^2$. The scatter plot of the backward propagating diffracted SHG corresponding to the fundamental excitation resonance at 1572 nm is shown in the inset of Fig. 4(a). The diffraction pattern is color-coded based on the SHG signal strength in the respective orders for the nonlinear polarization shown in Figs. 3(e)–3(g). The diffraction orders with significant SHG energy are found to be the zeroth-order along the optical axis, and the higher-orders arranged in the hexagonal pattern at identical polar diffraction angles of 49.1°, calculated using the diffraction equation [37]. The diffraction orders are labeled with two indices corresponding to the representation of the hexagonal lattice as repetitive rectangular unit cells with periodicity (Λ, $\sqrt{3}\Lambda$), with silicon pillars located at the center and four corners. Figure 4(b) shows the SHG polar plot for the native GaSe layer in the absence of the underlying metasurface. This is compared with polar plots of SHG signal calculated for each of the diffracted SHG orders as a function of varying incident fundamental polarization angle in Figs. 4(c)–4(f).

The polar plots are shown separately for the SHG signal polarized in the in-plane and out-of-plane directions with respect to the plane-of-diffraction by the blue and red curves, respectively. It is found that the zeroth order diffracted SHG being the DC component in terms of the spatial frequency content of the grating pattern results in polarization dependence which looks identical to the native GaSe layer. In contrast, the higher order diffracted SHG polar plots are found to be

Optics EXPRESS

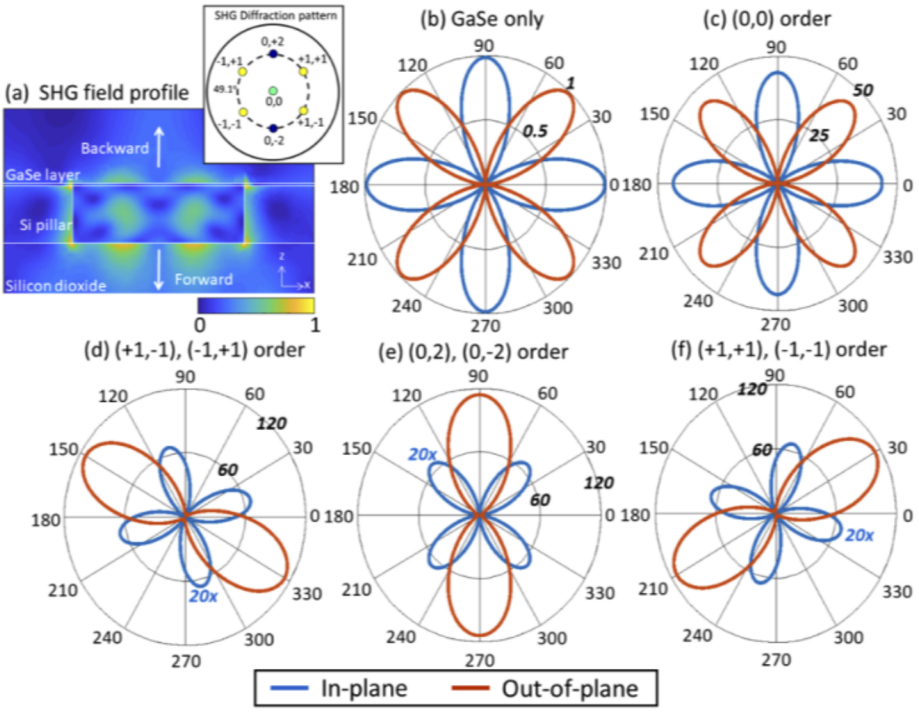

Fig. 4. (a) The SHG electric-field profile along xz-plane for 786 nm wavelength obtained by solving for the nonlinear wave propagation. The field is plotted across an area of 1.2×1.22 μm. The inset shows a scatter plot of the diffraction orders for backward propagating SHG. The corresponding diffraction angle for the higher orders is marked by the dashed circle. Polar plots showing SHG signal variation as a function of incident fundamental excitation polarization angle for: (b) GaSe layer without the metasurface, (c) (0,0), (d) (+1,-1), (-1,+1), (e) (0,2), (0,-2) and (f) (-1,+1), (+1,-1) diffracted waves. The blue and red-curves denote in-plane and out-of-plane oriented SHG signals with respect to the plane of diffraction.

very different from that of the native GaSe layer. The polar plots for the higher orders are also found to be rotated by 60° with respect to each other due to the hexagonal arrangement of the diffraction patterns, as shown in Fig. 4(a). For the circularly-symmetric meta-atom, the nonlinear polarization profiles shown in Figs. 3(e)–3(g) rotate with the incident fundamental polarization. There are characteristic incident polarization angles at which the SHG emission from adjacent meta-atoms coherently build up to give rise to maxima in the polar plots. Furthermore, the in-plane and out-of-plane polar plots show dominant four-fold and two-fold symmetry, which is a consequence of the four- and two-lobed SHG polarization profiles for y- and x- components, as shown in Figs. 3(e) and 3(f) respectively. It is concluded that polarization-independent SHG enhancement for the studied 2D material- resonant metasurface structures is achieved only for the zeroth-diffraction order. Thus, it is imperative to restrict the collection angles for the SHG signal to detect only the zeroth order diffraction, which is achieved by the choice of the objective lens used in the experiments, with acceptance angle less than the higher order diffraction angle of 49.1° as shown in Fig. 4(a).

The polarization dependence of SHG signals in odd-layer TMDC materials is often reported with characteristic six-fold symmetry [35]. These materials have the same crystal symmetry as ε-GaSe. The observed six-fold symmetry is due to the projection of the nonlinear polarization components on to the incident polarization direction. This is typically accomplished in experiments by either

Optics EXPRESS

rotating the analyzer along with the incident excitation polarization or by rotating the sample and keeping the incident polarizer and analyzer oriented parallel or perpendicular to each other. This is to be contrasted with the polarization study presented in this paper and reported previously [38], where the incident polarization is rotated keeping the analyzer oriented either parallel or perpendicular to the lab axes, thus resulting in the four-fold symmetry pattern as derived above. It is also pointed out that the above analysis treats both the excitation and collection as plane waves, while real experiments would make use of Gaussian beam-like excitation. Nonetheless, the above analysis is still valid for loosely focused gaussian spot illuminating multiple meta-atom elements at focus. This resembles multiple plane-wave excitations with reduced incidence angle spread and the corresponding SHG diffraction patterns with individual gaussian spots rather than ideal points, as shown in Fig. 4(a).

3. Device fabrication

The designed resonant structures are fabricated on a standard SOI substrate with top silicon layer of thickness 220 +/- 25 nm and a buried silicon dioxide layer of thickness 2 µm. The grating structures are first patterned using e-beam lithography technique with PMMA-C3 as the resist and subsequently dry etched using fluorine-based plasma chemistry. The top and perspective-view scanning electron microscopy (SEM) images of the final fabricated structures are shown in Figs. 5(a) and 5(b) respectively. The average dimensions of the fabricated metasurface are estimated as: pitch, $\Lambda = 1.2$ µm, diameter, $D = 660$ nm and height, $h = 220$ nm. GaSe flakes exfoliated from GaSe crystals (from 2D-Semiconductor, USA) were transferred onto polydimethylsiloxane (PDMS) substrate using scotch-tape transfer technique and subsequently transferred on top of the dielectric structure using dry transfer method. The optical microscopy and atomic force microscopy (AFM) images of the GaSe flake on top of the structures are shown in Figs. 5(c) and 5(d) respectively. From the line scan shown in the inset of Fig. 5(d), the thickness of the transferred flake used in the SHG studies is estimated to be ~10 nm, which consists of ~11 layers.

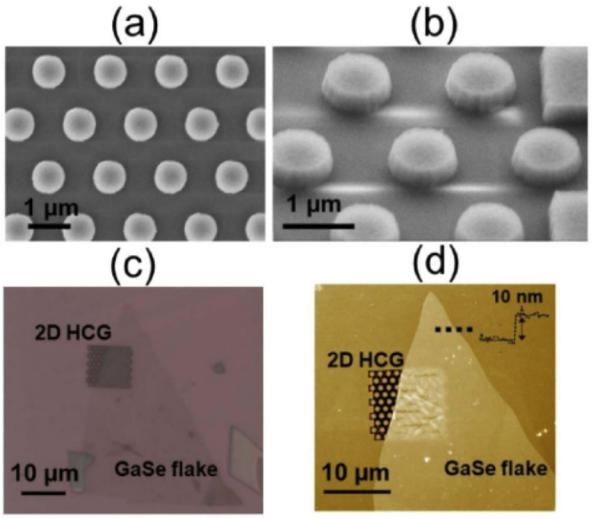

Fig. 5. (a) Top-view and (b) perspective-view SEM images of the fabricated resonant metasurface. (c) Optical microscopy image and (d) AFM image of the multilayer GaSe transferred on to the metasurface structure. The inset of (d) shows the line profile of the height map of the GaSe layer showing flake thickness of ~ 10 nm.

Optics EXPRESS

4. Experimental studies

The fabricated 2D material-resonant metasurface structures are experimentally characterized here by measuring the linear transmission spectrum, SHG enhancement and its polarization dependence. A schematic of the experimental set-up is shown in Fig. 6(a). For linear transmission studies, a continuous wave external-cavity tunable laser (Agilent 81600B) is loosely focused on to the sample placed on an Olympus inverted microscope (IX73). The incident light passes through an iris-aperture placed at the conjugate plane to the back focal plane of the objective before focusing using a 20x /0.75 numerical aperture (NA) objective lens. The partially closed aperture restricts the incident angles to ~12°. The transmitted signal collected using a germanium photodetector is normalized with respect to the transmission through a glass slide to plot the transmission spectrum as a function of the laser wavelength. The measured transmission spectra of the resonant metasurface with and without the GaSe flake are shown in Fig. 6(b). Transmission dips are observed at 1605 nm and 1630 nm for the measurements without and with the GaSe flake respectively. The Q-factor of the resonance in the presence of GaSe flake is extracted as 22. In the presence of the GaSe flake, the transmission spectrum is found to red-shift by ~25 nm with slight reduction in spectral width, consistent with the predictions of the simulations in Fig. 2(c). The red-shift of the experimental measurements when compared to the simulations is attributed to the discrepancy in the meta-atom dimensions, especially the thickness of the silicon layer due to large variations in the starting silicon film thickness. The measured wider spectral width (or lower Q-factor) and lower contrast when compared to simulations are attributed to the non-plane wave excitation at the fundamental wavelength, the finite size of the silicon metasurface [39] and fabrication induced surface/ edge roughness.

Next, SHG studies were performed in a conventional nonlinear optical microscopy platform [40], shown in the experimental set-up of Fig. 6(a). A wavelength tunable optical parametric oscillator (APE Levante-IR with 200 fsec pulse-width and 80 MHz repetition-rate) used as the fundamental excitation source is focused on the sample. The excitation angles are restricted to 12° using the same aperture used in the linear measurements. This ensures narrowing of the excitation angular range without compromising on the collection angles for the SHG signal. The narrow excitation angle results in collective excitation of ~8×5 rectangular unit-cells with periodicity (Λ, $\sqrt{3}\,\Lambda$). The backward emitted SHG signal from the sample is collected using the same objective lens. The choice of 0.75 NA objective lens with a collection angle of ~48.5° for these experiments ensures that the higher-order diffracted SHG signal is effectively rejected from the light collection path. The SHG signal is subsequently detected using a photomultiplier tube (PMT) with a combination of band-pass (Chroma, ET811/80) and short-pass (Thorlabs, FESH900 and Semrock, FF01-890) filters in front. The SHG signal is not spectrally resolved using a spectrometer in these experiments, but we rely on high efficiency filters in front of the PMT, similar to a conventional nonlinear optical microscopy system [40]. These filters ensure selective detection of SHG signal in the wavelength range of 770-850 nm with ~87% transmission and out-of-band rejection of the fundamental by ~120dB and 400-770 nm by 55 dB. The band-selective detection of nonlinear signals and the observed power dependence are used to confirm that the measured signal is SHG. Spatial mapping of SHG is performed by scanning the incident laser beam over a narrow angular range using scanning mirrors. For polarization studies, a half-wave plate and polarizer are used in the incident and detection path to rotate the incident linear polarization and analyze the detected SHG signal, respectively.

Figure 6(c) shows the SHG signal measured on- and off the resonant metasurface as a function of the incident laser wavelength for a fixed input power of ~4.8 mW average power. Maximum enhancement of ~22 times is obtained at 1645 nm excitation wavelength. The SHG enhancement factor is comparable to previous reports on GaSe layer on L-shaped asymmetric metasurfaces [25]. By taking the ratio of SHG signal and square of incident fundamental optical power at the sample plane, we estimate the maximum conversion efficiency of the SHG process to be

Optics EXPRESS

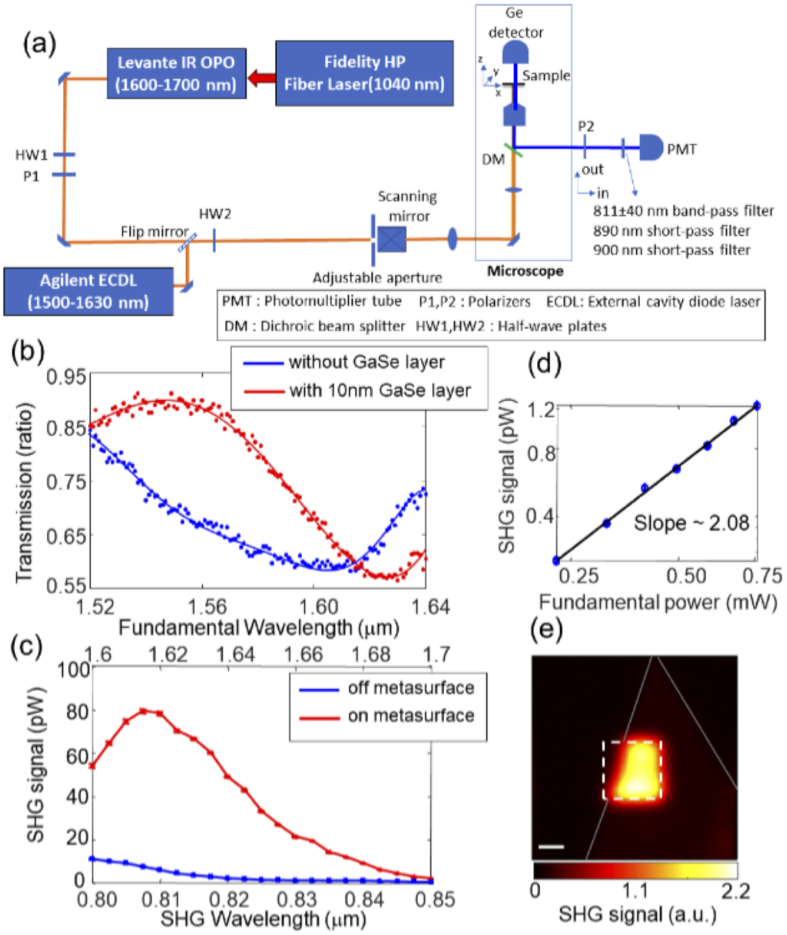

Fig. 6. (a) Schematic of the experimental set-up used for linear and non-linear optical measurements. (b) Linear transmission measurements measured for the silicon metasurface with (red curve) and without (blue curve) the GaSe layer. (c) SHG signal measured as a function of varying SHG and fundamental wavelength. Red and blue curves denote SHG signal from GaSe on top and away from the metasurface respectively. (d) Power dependence of the collected SHG signal as a function of incident fundamental optical power. The log-log plot shows a slope of 2.08. (e) SHG image obtained for the GaSe layer placed on top of the silicon metasurface at the fundamental wavelength of 1645 nm. Scale bar in the image is 5 μm.

$\sim 3.5 \times 10^{-4}$%/W. The Q-factor of the SHG spectrum is obtained as 30. We observe a clear narrowing of the SHG spectrum when compared to the linear transmission spectrum shown in Fig. 6(b) by a factor of ~1.345. This is consistent with the expected narrowing by a factor of 1.5 for the SHG spectrum when compared to the experimentally measured linear transmission spectrum.

The excitation power dependence of the detected signal is also shown in Fig. 6(d). The experimental data represented as a logarithmic plot shows linear dependence with a slope of 2.08, confirming the SHG process. SHG image at the maximum enhancement wavelength of 1645 nm for the GaSe layer above the metasurface is shown in Fig. 6(e). This image clearly shows strong SHG signal on top of the metasurface when compared to the flake outside the metasurface.

Optics EXPRESS

Polarization dependence of the SHG signal is studied by rotating the input excitation polarization and by collecting the polarized SHG signal with an analyzer placed in front of the PMT oriented along the in-plane and out-of-plane directions. The in-plane and out-of-plane directions of the analyzer are aligned parallel to x and y lab co-ordinate axes respectively. Figures 7(a) and 7(b) shows the SHG signal polar plots as a function of the incident polarization angle for GaSe layer with and without the underlying metasurface respectively. The experimentally obtained polar plots for SHG oriented in-plane and out-of-plane are shown by the blue and red colored data points respectively. The theoretical fit shown by the black curves corresponds to the zeroth-order diffracted SHG signal collected, as described in Fig. 4. An offset angle of $\phi = -13°$ between the lab x-axis and arm-chair axis is used to align the theoretical and experimental curve. Good agreement is obtained between the experimental data and theoretical fit for the polar plots with and without the metasurface. This confirms that the selective detection of the zeroth-order diffracted SHG by experimentally restricting the collection angle ensures that the polarization properties of SHG from 2D material-dielectric metasurface structures closely follows that of the native 2D material.

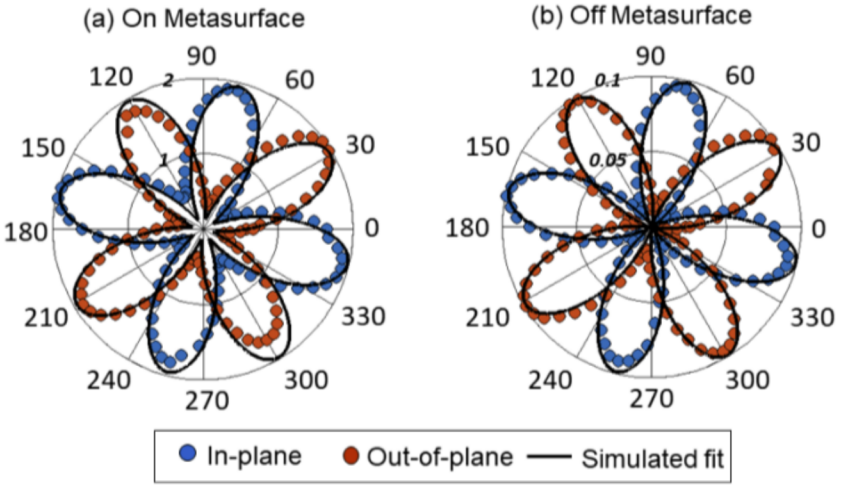

Fig. 7. Polarization dependence of the SHG signal as a function of varying incident fundamental polarization angle. The plots show SHG signal from the GaSe layer: (a) on top of the metasurface and (b) away from the metasurface. The blue and red circles denote the in-plane and out-of-plane SHG signals with respect to the plane of incidence. The in-plane and out-of-plane orientations correspond to the x and y lab-axes respectively for the zeroth-order diffracted SHG signal. The solid black curve represents simulated fits to the experimental data.

5. Conclusions

In this paper, polarization-independent, second harmonic generation enhancement from multilayer GaSe coupled to silicon-based resonant metasurface is reported by selectively detecting the zeroth-order diffracted SHG signal. The fabricated structures show resonant feature in the transmission spectrum in the 1600 nm wavelength range, which narrows and red-shifts with the addition of the multilayer GaSe. Polarization studies of SHG emission from the GaSe flake on- and off- the gratings show that the polarization properties of the GaSe layer remains unaffected by the underlying metasurface when selectively detecting the zeroth-order diffracted SHG. Polarization-independent enhancement of nonlinear optical effects in heterogeneously integrated metasurface

Optics EXPRESS

presents an attractive approach towards realizing robust, nonlinear photonic functionalities without altering the inherent properties of the 2D material or requiring precise alignment of the 2D material with the underlying photonic structure. This work underscores that it is not sufficient to merely use symmetric meta-atoms in such heterogeneously integrated systems for achieving polarization independent enhancement of nonlinear signal. A thorough consideration of depolarization and higher-order diffraction effects is required, and true polarization independent enhancement is achieved only for the zeroth-order diffracted nonlinear signal. Even though the quality factor of the resonant structures considered here are modest, an understanding of the role of depolarization and higher order diffraction effects in achieving polarization independent nonlinear optical enhancement are important irrespective of quality factor of the resonances. Higher quality factor resonances as proposed in previous reports [10,11,25] can further help in achieving higher enhancement factors for the nonlinear optical signal. However, achieving polarization independence in such structures is still an open question.

Funding

Ministry of Electronics and Information technology (MeITY Quantum program); Department of Science and Technology, Ministry of Science and Technology, India (QUST program).

Acknowledgments

The fabrication and some characterization work were carried out at the National Nanofabrication Centre (NNFC) and Micro Nano Characterization Facility (MNCF) respectively, located at the Centre for Nano Science and Engineering (CeNSE), Indian Institute of Science, Bangalore.

Disclosures

The authors declare no conflicts of interest.

References

1. A. E. Krasnok, A. E. Miroshnichenko, P. A. Belov, and Y. S. Kivshar, "All-dielectric optical nanoantennas," Opt. Express **20**(18), 20599–20604 (2012).
2. A. I. Kuznetsov, A. E. Miroshnichenko, M. L. Brongersma, Y. S. Kivshar, and B. Luk'yanchuk, "Optically resonant dielectric nanostructures," Science **354**(6314), aag2472 (2016).
3. A. Arbabi, Y. Horie, M. Bagheri, and A. Faraon, "Dielectric metasurfaces for complete control of phase and polarization with subwavelength spatial resolution and high transmission," Nat. Nanotechnol. **10**(11), 937–943 (2015).
4. R. Paniagua-Domínguez, Y. F. Yu, and A. E. Miroshnichenko, "Generalized Brewster effect in dielectric metasurfaces," Nat. Commun. **7**(1), 10362 (2016).
5. P. R. West, J. L. Stewart, A. V. Kildishev, V. M. Shalaev, V. V. Shkunov, F. Strohkendl, Y. A. Zakharenkov, R. K. Dodds, and R. Byren, "All-dielectric subwavelength metasurface focusing lens," Opt. Express **22**(21), 26212–26221 (2014).
6. M. Khorasaninejad, F. Aieta, P. Kanhaiya, M. A. Kats, P. Genevet, D. Rousso, and F. Capasso, "Achromatic Metasurface Lens at Telecommunication Wavelengths," Nano Lett. **15**(8), 5358–5362 (2015).
7. B. Wang, F. Dong, Q. Li, D. Yang, C. Sun, J. Chen, Z. Song, L. Xu, W. Chu, Y. Xiao, Q. Gong, and Y. Li, "Visible-Frequency Dielectric Metasurfaces for Multiwavelength Achromatic and Highly Dispersive Holograms," Nano Lett. **16**(8), 5235–5240 (2016).
8. R. C. Devlin, M. Khorasaninejad, W. T. Chen, J. Oh, and F. Capasso, "Broadband high-efficiency dielectric metasurfaces for the visible spectrum," Proc. Natl. Acad. Sci. **113**(38), 10473–10478 (2016).
9. S. Liu, M. B. Sinclair, S. Saravi, G. A. Keeler, Y. Yang, J. Reno, G. M. Peake, F. Setzpfandt, I. Staude, T. Pertsch, and I. Brener, "Resonantly Enhanced Second-Harmonic Generation Using III-V Semiconductor All-Dielectric Metasurfaces," Nano Lett. **16**(9), 5426–5432 (2016).
10. Y. Yang, W. Wang, A. Boulesbaa, I. I. Kravchenko, D. P. Briggs, A. Puretzky, D. Geohegan, and J. Valentine, "Nonlinear Fano-Resonant Dielectric Metasurfaces," Nano Lett. **15**(11), 7388–7393 (2015).
11. S. Liu, P. P. Vabishchevich, A. Vaskin, J. L. Reno, G. A. Keeler, M. B. Sinclair, I. Staude, and I. Brener, "An all-dielectric metasurface as a broadband optical frequency mixer," Nat. Commun. **9**(1), 2507 (2018).

Optics EXPRESS

12. Y. Zhou, M. C. Y. Huang, C. Chase, V. Karagodsky, M. Moewe, B. Pesala, F. G. Sedgwick, and C. J. Chang-Hasnain, "High-Index-Contrast Grating (HCG) and Its Applications in Optoelectronic Devices," IEEE J. Sel. Top. Quantum Electron. **15**(5), 1485–1499 (2009).
13. R. Magnusson, "Wideband reflectors with zero-contrast gratings," Opt. Lett. **39**(15), 4337–4340 (2014).
14. R. Biswas, J. Deka, K. k. Jha, A. V. Praveen, A. S. L. Krishna, S. Menon, and V. Raghunathan, "Resonant four-wave mixing microscopy on silicon-on-insulator based zero-contrast gratings," OSA Continuum **2**(10), 2864–2874 (2019).
15. G. Grinblat, Y. Li, M. P. Nielsen, R. F. Oulton, and S. A. Maier, "Degenerate Four-Wave Mixing in a Multiresonant Germanium Nanodisk," ACS Photonics **4**(9), 2144–2149 (2017).
16. M. R. Shcherbakov, D. N. Neshev, B. Hopkins, A. S. Shorokhov, I. Staude, E. V. Melik-Gaykazyan, M. Decker, A. A. Ezhov, A. E. Miroshnichenko, I. Brener, A. A. Fedyanin, and Y. S. Kivshar, "Enhanced Third-Harmonic Generation in Silicon Nanoparticles Driven by Magnetic Response," Nano Lett. **14**(11), 6488–6492 (2014).
17. M. R. Shcherbakov, A. S. Shorokhov, D. N. Neshev, B. Hopkins, I. Staude, E. V. Melik-Gaykazyan, A. A. Ezhov, A. E. Miroshnichenko, I. Brener, A. A. Fedyanin, and Y. S. Kivshar, "Nonlinear Interference and Tailorable Third-Harmonic Generation from Dielectric Oligomers," ACS Photonics **2**(5), 578–582 (2015).
18. A. Autere, H. Jussila, Y. Dai, Y. Wang, H. Lipsanen, and Z. Sun, "Nonlinear Optics with 2D Layered Materials," Adv. Mater. **30**(24), 1705963 (2018).
19. T. K. Fryett, K. L. Seyler, J. Zheng, C. Liu, X. Xu, and A. Majumdar, "Silicon photonic crystal cavity enhanced second-harmonic generation from monolayer WSe2," 2D Mater. **4**(10), 015031 (2017).
20. X. Gan, C. Zhao, S. Hu, T. Wang, Y. Song, J. Li, Q. Zhao, W. Jie, and J. Zhao, "Microwatts continuous-wave pumped second harmonic generation in few- and mono-layer GaSe," Light: Sci. Appl. **7**(1), 17126 (2018).
21. L. Fang, Q. Yuan, H. Fang, X. Gan, J. Li, T. Wang, Q. Zhao, W. Jie, and J. Zhao, "Multiple Optical Frequency Conversions in Few-Layer GaSe Assisted by a Photonic Crystal Cavity," Adv. Opt. Mater. **6**(22), 1800698 (2018).
22. J. K. Day, M. Chung, Y. Lee, and V. M. Menon, "Microcavity enhanced second harmonic generation in 2D MoS2," Opt. Mater. Express **6**(7), 2360–2365 (2016).
23. F. Yi, M. Ren, J. C. Reed, H. Zhu, J. Hou, C. H. Naylor, A. T. C. Johnson, R. Agarwal, and E. Cubukcu, "Optomechanical Enhancement of Doubly Resonant 2D Optical Nonlinearity," Nano Lett. **16**(3), 1631–1636 (2016).
24. Z. Wang, Z. Dong, H. Zhu, L. Jin, M. Chiu, L. Li, Q. Xu, G. Eda, S. A. Maier, A. T. S. Wee, C. Qiu, and J. K. W. Yang, "Selectively Plasmon-Enhanced Second-Harmonic Generation from Monolayer Tungsten Diselenide on Flexible Substrates," ACS Nano **12**(2), 1859–1867 (2018).
25. Q. Yuan, L. Fang, H. Fang, J. Li, T. Wang, W. Jie, J. Zhao, and X. Gan, "Second Harmonic and Sum-Frequency Generations from a Silicon Metasurface Integrated with a Two-Dimensional Material," ACS Photonics **6**(9), 2252–2259 (2019).
26. T. Wang and S. Zhang, "Large enhancement of second harmonic generation from transition-metal dichalcogenide monolayer on grating near bound states in the continuum," Opt. Express **26**(1), 322–337 (2018).
27. X. Zhou, J. Cheng, Y. Zhou, T. Cao, H. Hong, Z. Liao, S. Wu, H. Peng, K. Liu, and D. Yu, "Strong Second-Harmonic Generation in Atomic Layered GaSe," J. Am. Chem. Soc. **137**(25), 7994–7997 (2015).
28. K. R. Allakhverdiev, MÖ Yetis, S. Özbek, T. K. Baykara, and E. Y. Salaev, "Effective nonlinear GaSe crystal. Optical properties and applications," Laser Phys. **19**(5), 1092–1104 (2009).
29. W. Jie, X. Chen, D. Li, L. Xie, Y. Y. Hui, S. P. Lau, X. Cui, and J. Hao, "Layer-dependent nonlinear optical properties and stability of non-centrosymmetric modification in few-layer GaSe sheets," Angew. Chem. **127**(4), 1201–1205 (2015).
30. V. Liu and S. Fan, "S4: A free electromagnetic solver for layered periodic structures," Comput. Phys. Commun. **183**(10), 2233–2244 (2012).
31. P. Qiao, L. Zhu, W. C. Chew, and C. J. Chang-Hasnain, "Theory and design of two-dimensional high-contrast-grating phased arrays," Opt. Express **23**(19), 24508–24524 (2015).
32. K. Kato, F. Tanno, and N. Umemura, "Sellmeier and thermo-optic dispersion formulas for GaSe (Revisited)," Appl. Opt. **52**(11), 2325–2328 (2013).
33. L. Novotny and B. Hecht, *Principles of Nano-optics*, (Cambridge University, Rochester, New York, 2006), pp. 45–88.
34. R. W. Boyd, *Nonlinear optics*, (Academic Press, Rochester, New York, 2008).
35. Y. Li, Y. Rao, K. F. Mak, Y. You, S. Wang, C. R. Dean, and T. F. Heinz, "Probing Symmetry Properties of Few-Layer MoS2 and h-BN by Optical Second-Harmonic Generation," Nano Lett. **13**(7), 3329–3333 (2013).
36. COMSOL, Wave optics module, User Guide. https://doc.comsol.com/5.5/
37. E. G. Loewen and E. Popov, *Diffraction gratings and applications*, (CRC Taylor & Francis, New York, 1997).
38. H. D. Saleh, S. Vezzoli, L. Caspani, A. Branny, S. Kumar, B. D. Gerardot, and D. Faccio, "Towards spontaneous parametric down conversion from monolayer MoS2," Sci. Rep. **8**(1), 3862 (2018).
39. R. R. Boye and R. K. Kostuk, "Investigation of the effect of finite grating size on the performance of guided-mode resonance filters," Appl. Opt. **39**(21), 3649–3653 (2000).
40. F. S. Pavone and P. J. Campagnola (Eds.), *Second Harmonic Generation Imaging*, 1st Edition, (CRC Press, Boca Raton, Florida, 2016).